

Novel UiO-NH₂-like Zr-Based MOF (Basu-DPU) as an Excellent Catalyst for Preparation of New 6*H*-Chromeno[4,3-*b*]quinolin-6-ones

Masoumeh Beiranvand, Davood Habibi,* and Hosein Khodakarami

Cite This: *ACS Omega* 2023, 8, 25924–25937

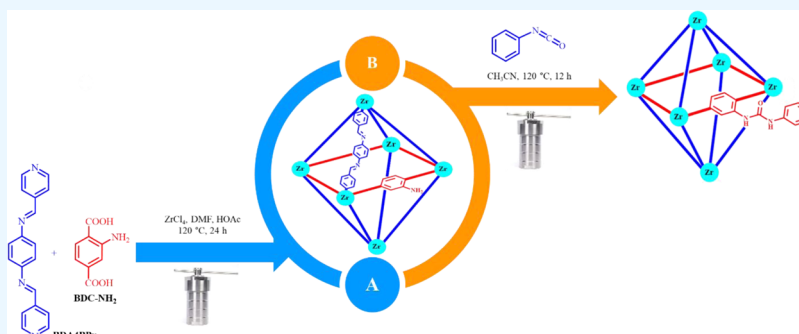
Read Online

ACCESS |

Metrics & More

Article Recommendations

Supporting Information



ABSTRACT: A new two-fold interpenetrated pillar-layered metal–organic framework (MOF) was designed and synthesized based on zirconium cations, an amine-functionalized ligand, and a linear *exo*-bidentate bis-pyridine ligand. The structure of the prepared framework was evaluated using various techniques, such as Fourier transform infrared (FTIR), ¹³C NMR, energy-dispersive X-ray (EDX), elemental mapping analysis, scanning electron microscopy (SEM), X-ray diffraction (XRD), thermogravimetric analysis/differential thermal analysis (TGA/DTA), and Brunauer–Emmett–Teller (BET). Then, catalytic application of the prepared zirconium-based MOF was successfully explored in the synthesis of novel 6*H*-chromeno[4,3-*b*]quinolin-6-ones **4(a–I)** through a one-pot three-component condensation reaction of 4-hydroxycumarine, 1-naphthylamine, and aromatic aldehydes under solvent-free conditions at 110 °C. The pure products were obtained with high atom efficiency (AE) and short reaction times and characterized by FTIR, NMR, and mass spectrometry techniques.

1. INTRODUCTION

Metal–organic frameworks (MOFs), known as porous coordination networks (PCNs), are a class of functional meso-/microporous crystalline materials constituted by the auto-assembly of metal ions or metal oxide clusters and organic ligands through covalent connection.¹ Ultrahigh surface area, praiseworthy porous texture, various pore sizes and shapes, and appropriate thermal and mechanical stabilities in the MOFs allow multiple applications in gas adsorption, chemical separation, catalysis processes, electronic and optoelectronic devices, drug delivery, nonlinear optical (NLO) materials, and so on.^{2–15}

One of the most creditable and controlled strategies to build 3D porous frameworks is the pillaring strategy because this approach applies size-alterable organic linkers for systematically adjusting pore size and shape and functional groups embedded in the ligands in pillars or layers for modulating the pore surface toward the desired properties. The layer structural motif pillar-layered MOFs are usually not affected by the pillar change. Due to the high ability of the rigid carboxylate ligands to adopt various bonding modes and satisfy different metal coordination preferences, one rational methodology to fabricate these structures is to utilize rigid carboxylate ligands

to bridge two-dimensional (2D) layers organized by metal ions and amines.^{16,17} Modifying the pillars can lead to control of hydrophilic/hydrophobic character, hydrogen bonding, and open metal site of the available frameworks.¹⁸

Among subclasses of MOFs, zirconium-based MOFs (Zr-MOFs) stand out due to the strong Zr–O coordination bond, practicable synthetic conditions, and facility of reproducibility. The strong Zr–O coordination bond, along with the robust polynuclear molecular building blocks, causes Zr-MOFs an exceptional family of structures that are promising because of their tenability, stability, and design ability.^{19–21}

Chromeno quinolines display remarkable properties in biological, medicinal, and fluorescence areas (Figure 1).²²

Despite the significant role of fused chromeno quinolines in modern chemistry, efficient synthetic methods for their

Received: March 16, 2023

Accepted: June 21, 2023

Published: July 12, 2023



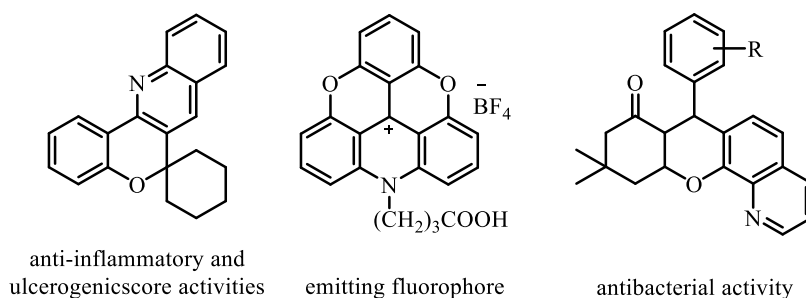
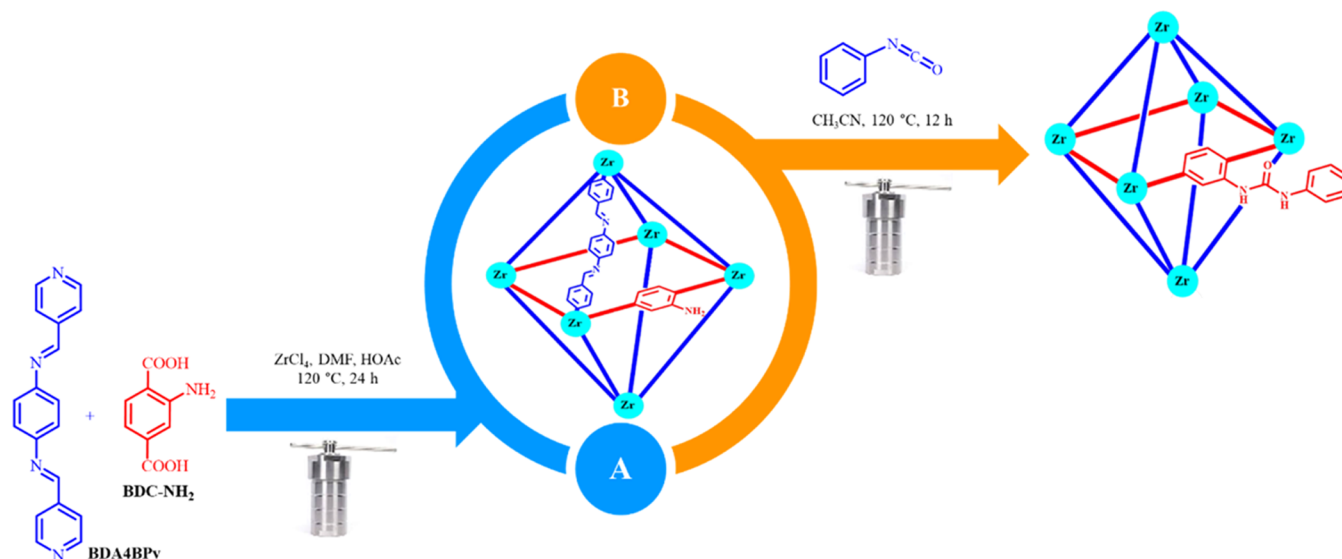
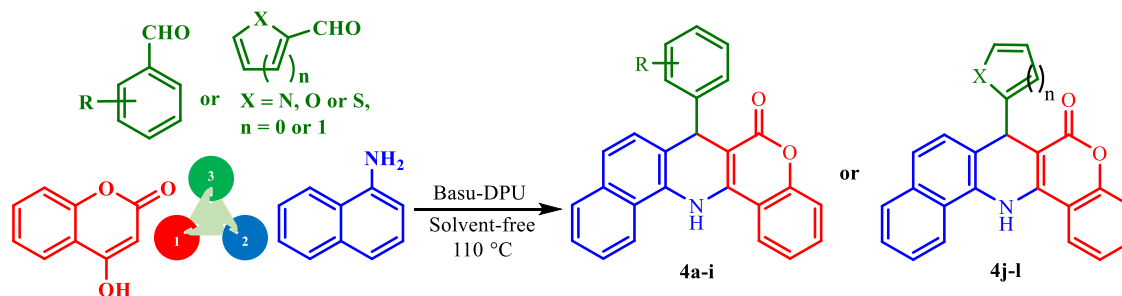


Figure 1. Biologically active chromenoquinolines.

Scheme 1. Synthesis of the Basu-DPU Framework



Scheme 2. Synthesis of 4(a-1)



synthesis have rarely been presented. In general, the reported synthetic strategies for the synthesis of 6*H*-chromeno[4,3-*b*]quinolin-6-ones used the Vilsmeier reagent or formyl group of aromatic aldehydes as the source of the methine (CH) group in the quinoline ring.²³ For example, a study reported by Hegab et al. described an efficient synthesis of 6,6-disubstituted chromeno[4,3-*b*]- and chromeno-[3,4-*c*]-quinolines employing the Vilsmeier reagent.²⁴ Wang and co-workers presented a condensation of 4-hydroxycoumarin and *N*-arylidene-naphthalen-2-amine in aqueous media catalyzed by TEBAC to give 7-aryl-7,14-dihydro-6*H*-benzo[*f*]chromeno[4,3-*b*]-quinolin-6-ones in good to high yields.²⁵ Weng et al. reported the metal-catalyst-free electro-oxidative cyclization of 4-(phenylamino)-2*H*-chromen-2-ones for their synthesis using DMF as the methine group.²⁶ Several reports have been established for their synthesis through a three-component

condensation of 4-hydroxycoumarin, aldehydes, and aromatic amines catalyzed by ([HYSBPI]HSO₄) and graphene oxide, bismuth triflate, and Fe₃O₄@SiO₂@CPS.^{27–30}

This work aimed to synthesize, characterize, and explore the potential of a new Zr-MOF [Zr(BDA4BPY)(BDC-NH₂)-(PhNCO)] (Basu-DPU) (Scheme 1).

Then, it was used as a capable catalyst for the synthesis of 4(a-1) by the three-component condensation reaction of 4-hydroxycoumarin, 1-naphthylamine, and aromatic aldehydes (Scheme 2).

2. EXPERIMENTAL SECTION

2.1. General. All of the commercial reagents were provided by the Merck or Aldrich Chemical companies and applied without further purification. The reaction progression and purity of the prepared compounds were monitored by thin-

layer chromatography (TLC) performed with silica gel 60 F-254 plates. Fourier transform infrared (FTIR) spectra were recorded on a Perkin Elmer Spectrum Version 10.02.00 employing KBr pellets. The ^1H NMR (250 MHz) and ^{13}C NMR (62.5 MHz) spectra were taken on a Bruker spectrometer (δ in ppm) using $\text{DMSO-}d_6$ as a solvent with chemical shifts measured relative to TMS as the internal standard. Melting points were taken with a BUCHI 510 melting point apparatus. Elemental analysis was performed using a MIRA II analyzer. The field-emission scanning electron microscopy (FESEM) images were recorded using a MIRA III analyzer. The X-ray diffraction (XRD) measurements were carried out with an XRD Philips PW1730. Thermogravimetric-differential thermal analysis (TGA-DTA) was done using an SDT-Q600 device. The mass spectra were recorded on an Agilent mass spectrometer (HP), model: 5973 network mass selective detector, ion source: electron impact (EI) 70 eV, ion source temperature: 230 $^\circ\text{C}$, with a quadrupole analyzer.

2.2. General Strategy for the Fabrication of the Basu-DPU Framework. Basu-DPU was synthesized in the following three sequential steps:

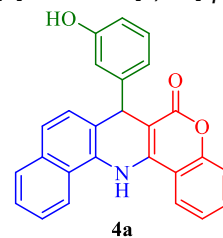
Stage 1: The *exo*-bidentate N^1, N^4 -bis(pyridin-4-ylmethylene)-benzene-1,4-diamine (BDA4BPY) ligand was synthesized based on the literature.³¹ Briefly, the mixture of 4-pyridine-carbaldehyde (20 mmol) and 1,4-benzenediamine (10 mmol) was refluxed in toluene in the presence of piperidine (0.1 mL) as a catalyst for 2 h. Then, the obtained yellow precipitate was filtered, recrystallized in ethanol (yield: 90%), and characterized by FTIR analysis.

Stage 2: $[\text{Zr}(\text{BDA4BPY})(\text{BDC-NH}_2)]$ (Basu) was prepared by the solvothermal procedure. ZrCl_4 (1.2 mmol), BDA4BPY ligand (0.3 mmol), and 2-aminoterephthalic acid (BDC-NH_2) (0.5 mmol) were mixed in DMF (20 mL) and stirred for 15 min at room temperature. Then, acetic acid (20 mL) was added, and the mixture was placed in a Teflon reactor and put in an oven at 120 $^\circ\text{C}$ for 24 h. The mixture was then allowed to cool slowly to room temperature, centrifuged, washed with DMF and ethanol to give the cream-colored Basu, and characterized by FTIR, energy-dispersive X-ray (EDX), elemental mapping, XRD, SEM, and Brunauer–Emmett–Teller (BET) analyses.

Stage 3: Further functionalization of Basu was carried out with phenyl isocyanate according to the literature.³² Briefly, Basu (200 mg) was dispersed in CH_3CN (10 mL) and reacted with phenyl isocyanate (5 mmol). The resulting mixture was placed in a Teflon reactor and put in an oven at 120 $^\circ\text{C}$ for 12 h. Finally, the cream solid was centrifuged, washed with CH_3CN , and vacuum dried at 80 $^\circ\text{C}$ for 48 h to obtain the title postmodified MOF (Basu-DPU) and characterized by FTIR, EDX, elemental mapping, XRD, SEM, and BET analyses.

2.3. General Procedure for the Synthesis of 4(a–l) Catalyzed by Basu-DPU. 4-Hydroxycoumarin (1 mmol), 1-naphthylamine (1 mmol), aromatic aldehydes (1 mmol), and Basu-DPU (0.01 g) were mixed and stirred under solvent-free conditions at 110 $^\circ\text{C}$. After completion of the reaction (TLC: *n*-hexane/EtOAc), the solid was dissolved in DMF (10 mL) and centrifuged to separate the catalyst. Then, the product was washed with ethanol and acetone, purified by recrystallization in DMF or thin-layer chromatography plates, and characterized by FTIR, NMR, and mass spectrometry techniques.

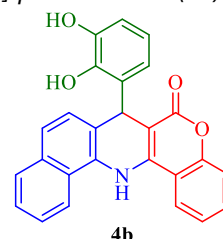
2.4. Spectral Data. 2.4.1. 7-(3-Hydroxyphenyl)-7,14-dihydro-6H-benzo[h]chromeno[4,3-b]quinolin-6-one (4a).



4a

Yellow solid, mp > 300 $^\circ\text{C}$, IR (KBr, cm^{-1}): 3438, 3269, 3060, 2893, 1661, 1517, 1468, and 1265. ^1H NMR (250 MHz, $\text{DMSO-}d_6$): δ = 9.45 (s, 1H), 9.22 (s, 1H), 8.62 (d, J = 8.4 Hz, 1H), 8.55 (d, J = 8.0 Hz, 1H), 7.85 (d, J = 8.0 Hz, 1H), 7.65–7.58 (m, 2H), 7.54 (d, J = 7.3 Hz, 2H), 7.38 (q, J = 11.0 Hz, 3H), 6.99 (t, J = 7.8 Hz, 1H), 6.74 (d, J = 7.6 Hz, 1H), 6.67 (s, 1H), 6.50 (d, J = 5.7 Hz, 1H), 5.27 (s, 1H). ^{13}C NMR (62.5 MHz, $\text{DMSO-}d_6$) δ = 160.95, 157.85, 152.72, 148.58, 144.29, 133.05, 132.27, 130.48, 129.74, 128.64, 127.82, 126.54, 126.41, 124.38, 124.17, 123.91, 123.19, 122.27, 120.98, 118.47, 117.19, 114.67, 114.12, 113.93, 99.06, 41.89, 40.97, 40.64, 40.31, 39.97, 39.64, 39.30, 38.97. MS: ESI-mass: m/z = 391.

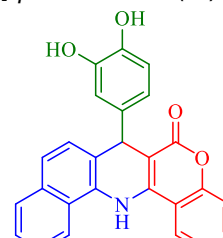
2.4.2. 7-(2,3-Dihydroxyphenyl)-7,14-dihydro-6H-benzo[h]chromeno[4,3-b]quinolin-6-one (4b).



4b

Cream solid, mp 280–283 $^\circ\text{C}$, IR (KBr, cm^{-1}): 3378, 3047, 1646, 1520, 1472, and 1264. ^1H NMR (250 MHz, $\text{DMSO-}d_6$) δ = 9.29 (d, J = 13.8 Hz, 2H), 8.65–8.45 (m, 3H), 7.81 (d, J = 7.8 Hz, 1H), 7.67–7.34 (m, 7H), 6.57–6.31 (m, 3H), 5.79 (s, 1H). ^{13}C NMR (62.5 MHz, $\text{DMSO-}d_6$) δ = 161.00, 152.71, 145.59, 145.07, 141.97, 135.14, 132.94, 132.19, 129.98, 128.52, 127.55, 126.28, 124.13, 123.89, 123.14, 122.17, 119.52, 119.23, 117.15, 114.09, 113.71, 98.92, 40.96, 40.63, 40.30, 39.96, 39.63, 39.30, 38.96, 34.91. MS: ESI-mass: m/z = 407.

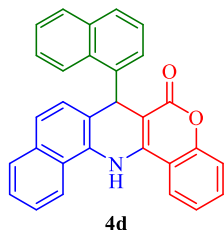
2.4.3. 7-(3,4-Dihydroxyphenyl)-7,14-dihydro-6H-benzo[h]chromeno[4,3-b]quinolin-6-one (4c).



4c

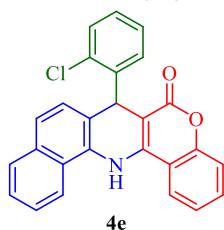
Cream solid, mp > 300 $^\circ\text{C}$, IR (KBr, cm^{-1}): 3511, 3439, 3027, 2885, 1659, 1523, 1472, and 1265. ^1H NMR (250 MHz, $\text{DMSO-}d_6$) δ = 9.42 (s, 1H), 8.70–8.52 (m, 4H), 7.87 (d, J = 8.0 Hz, 1H), 7.66–7.51 (m, 4H), 7.47–7.30 (m, 3H), 6.58 (d, J = 22.5 Hz, 3H), 5.17 (s, 1H). ^{13}C NMR (62.5 MHz, $\text{DMSO-}d_6$) δ = 160.97, 152.66, 145.43, 144.41, 143.93, 138.54, 132.96, 132.17, 130.34, 128.63, 127.92, 126.38, 124.17, 123.85, 123.35, 122.24, 121.76, 118.51, 117.17, 115.74, 115.24, 114.21, 99.49, 40.95, 40.63, 40.29, 39.96, 39.63, 39.29, 38.96. ESI-mass: m/z = 407.

2.4.4. 7-(Naphthalen-1-yl)-7,14-dihydro-6H-benzo[h]-chromeno[4,3-b]quinolin-6-one (**4d**).



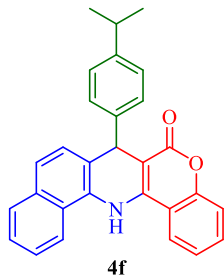
Cream solid, mp > 300 °C, IR (KBr, cm^{-1}): 3358, 3035, 1665, 1620, 1522, 1477, and 1267. ^1H NMR (250 MHz, $\text{DMSO}-d_6$) δ = 9.46 (s, 1H), 8.79 (d, J = 8.6 Hz, 1H), 8.62 (t, J = 10.1 Hz, 2H), 7.88 (d, J = 8.0 Hz, 1H), 7.77 (d, J = 7.8 Hz, 1H), 7.63 (q, J = 7.5 Hz, 4H), 7.52 (d, J = 7.4 Hz, 3H), 7.40 (d, J = 8.6 Hz, 4H), 7.16 (d, J = 8.3 Hz, 1H), 6.25 (s, 1H). ^{13}C NMR (62.5 MHz, $\text{DMSO}-d_6$) δ = 152.73, 145.55, 144.53, 133.78, 132.99, 132.33, 130.78, 129.84, 128.58, 126.81, 126.44, 124.53, 124.13, 123.32, 122.40, 121.85, 117.16, 114.02, 100.07, 40.97, 40.64, 40.30, 39.97, 39.64, 39.30, 38.97, 37.02. ESI-mass: m/z = 425.

2.4.5. 7-(2-Chlorophenyl)-7,14-dihydro-6H-benzo[h]-chromeno[4,3-b]quinolin-6-one (**4e**).



Cream solid, mp > 300 °C, IR (KBr, cm^{-1}): 3321, 3060, 1662, 1618, 1520, 1470, and 1271. ^1H NMR (250 MHz, $\text{DMSO}-d_6$) δ = 9.38 (s, 1H), 8.58 (dd, J = 13.2, 8.3 Hz, 2H), 7.82 (d, J = 8.1 Hz, 1H), 7.64 (d, J = 8.6 Hz, 2H), 7.52 (dd, J = 11.7, 7.8 Hz, 4H), 7.38 (d, J = 8.1 Hz, 2H), 7.27 (d, J = 8.6 Hz, 1H), 7.17–7.09 (m, 2H), 5.89 (s, 1H). ^{13}C NMR (62.5 MHz, $\text{DMSO}-d_6$) δ = 152.84, 145.27, 133.14, 132.50, 131.43, 131.06, 130.18, 129.80, 128.62, 128.25, 126.77, 126.54, 124.54, 124.18, 123.22, 122.43, 120.21, 117.21, 113.83, 40.94, 40.61, 40.28, 39.94, 39.61, 39.28, 39.06, 38.94. ESI-mass: m/z = 409.

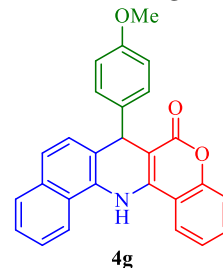
2.4.6. 7-(4-Isopropylphenyl)-7,14-dihydro-6H-benzo[h]-chromeno[4,3-b]quinolin-6-one (**4f**).



Yellow solid, mp > 300 °C, IR (KBr, cm^{-1}): 3353, 2957, 1665, 1620, 1524, 1479, and 1269. ^1H NMR (250 MHz, $\text{DMSO}-d_6$) δ = 9.49 (s, 1H), 8.60 (dd, J = 16.6, 8.2 Hz, 2H), 7.86 (d, J = 8.0 Hz, 2H), 7.58 (ddt, J = 25.4, 18.9, 8.3 Hz, 6H), 7.37 (t, J = 7.9 Hz, 2H), 7.19 (d, J = 7.8 Hz, 2H), 7.05 (d, J = 7.6 Hz, 2H), 5.32 (s, 1H), 2.72 (s, 1H), 1.07 (d, J = 6.9 Hz, 6H). ^{13}C NMR (62.5 MHz, $\text{DMSO}-d_6$) δ = 160.93, 156.74, 154.13, 152.71, 147.62, 147.00, 144.89, 139.41, 134.94, 132.27, 130.46, 128.62, 127.58, 126.78, 126.56, 124.45, 123.94, 121.66, 117.18, 40.97,

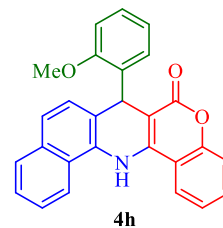
40.63, 40.30, 39.97, 39.63, 39.30, 38.97, 38.12, 33.40, 24.23. ESI-mass: m/z = 417.

2.4.7. 7-(4-Methoxyphenyl)-7,14-dihydro-6H-benzo[h]-chromeno[4,3-b]quinolin-6-one (**4g**).



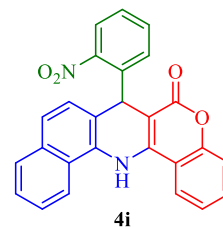
Yellow solid, mp > 300 °C, IR (KBr, cm^{-1}): 3294, 1665, 1622, 1522, 1400, and 1246. ^1H NMR (250 MHz, $\text{DMSO}-d_6$) δ = 9.44 (s, 1H), 8.59 (dd, J = 18.4, 8.2 Hz, 2H), 7.85 (d, J = 7.9 Hz, 1H), 7.66–7.31 (m, 7H), 7.17 (d, J = 8.2 Hz, 2H), 6.75 (d, J = 8.2 Hz, 2H), 5.30 (s, 1H), 3.61 (s, 3H). ^{13}C NMR (62.5 MHz, $\text{DMSO}-d_6$) δ = 160.93, 158.34, 152.72, 144.06, 139.67, 133.03, 132.22, 130.41, 128.74, 128.63, 127.87, 126.52, 126.40, 124.39, 124.14, 123.93, 123.20, 122.28, 121.25, 117.17, 114.25, 99.41, 55.42, 41.13, 41.01, 40.68, 40.34, 40.01, 39.68, 39.34, 39.01. ESI-mass: m/z = 405.

2.4.8. 7-(2-Methoxyphenyl)-7,14-dihydro-6H-benzo[h]-chromeno[4,3-b]quinolin-6-one (**4h**).



Yellow solid, mp > 300 °C, IR (KBr, cm^{-1}): 3347, 3063, 1665, 1620, 1520, 1471, and 1241. ^1H NMR (250 MHz, $\text{DMSO}-d_6$) δ = 9.37 (s, 1H), 8.58 (t, J = 7.7 Hz, 2H), 7.81 (d, J = 8.0 Hz, 1H), 7.61 (dd, J = 13.8, 7.7 Hz, 2H), 7.50 (dt, J = 8.4, 4.3 Hz, 3H), 7.38 (d, J = 8.4 Hz, 2H), 7.09 (t, J = 8.7 Hz, 2H), 6.94 (d, J = 8.0 Hz, 1H), 6.75 (t, J = 7.3 Hz, 1H), 5.77 (d, J = 2.6 Hz, 1H). ^{13}C NMR (62.5 MHz, $\text{DMSO}-d_6$) δ = 160.69, 156.15, 152.78, 145.24, 135.96, 132.93, 132.20, 130.24, 128.97, 128.51, 128.17, 127.28, 126.30, 124.12, 123.17, 122.23, 121.42, 121.16, 117.14, 114.07, 112.06, 98.49, 56.23, 40.98, 40.64, 40.31, 39.97, 39.64, 39.31, 38.98, 35.56. ESI-mass: m/z = 405.

2.4.9. 7-(2-Nitrophenyl)-7,14-dihydro-6H-benzo[h]-chromeno[4,3-b]quinolin-6-one (**4i**).



Orange solid, mp > 300 °C, IR (KBr, cm^{-1}): 3397, 2922, 1648, 1662, 1526, 1475, 1356, and 1265. ^1H NMR (250 MHz, $\text{DMSO}-d_6$) δ = 9.35 (s, 1H), 8.65 (d, J = 8.3 Hz, 1H), 8.55 (d, J = 7.9 Hz, 1H), 7.82 (s, 2H), 7.66–7.53 (m, 4H), 7.39 (d, J = 23.4 Hz, 6H), 6.02 (s, 1H). ^{13}C NMR (62.5 MHz, $\text{DMSO}-d_6$) δ = 162.72, 160.83, 152.74, 148.43, 144.15, 141.49, 133.98, 133.32, 132.55, 132.19, 130.81, 128.64, 128.07, 127.14, 126.96, 126.62, 124.87, 124.23, 123.73, 123.31, 122.50, 119.41, 117.21,

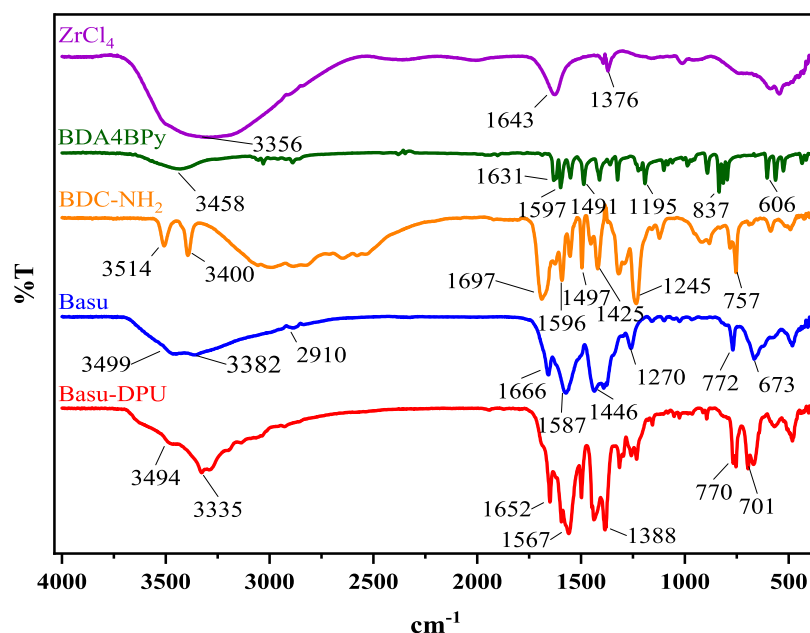


Figure 2. FTIR spectra of ZrCl_4 , BDA4BPy, BDC-NH₂, Basu, and Basu-DPU.

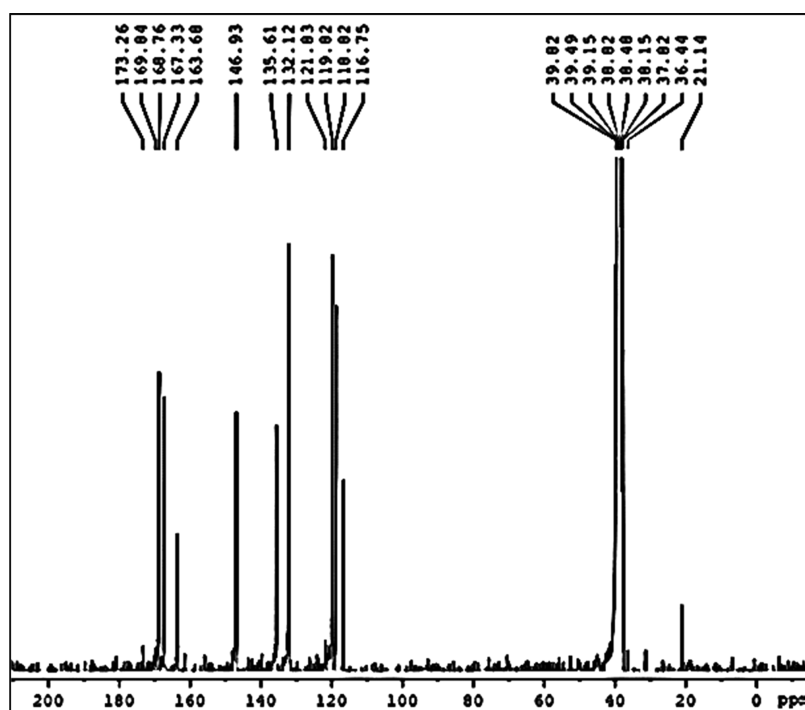
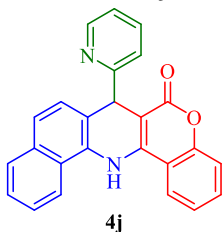


Figure 3. ¹³C NMR spectra of Basu.

113.74, 99.19, 41.00, 40.66, 40.33, 39.99, 39.66, 39.33, 38.99, 36.18, 31.19. ESI-mass: $m/z = 420$.

2.4.10. 7-(Pyridin-2-yl)-7,14-dihydro-6H-benzo[*h*]-chromeno[4,3-*b*]quinolin-6-one (**4j**).



Brown solid, mp > 300 °C, IR (KBr, cm^{-1}): 3421, 3047, 1683, 1638, 1590, 1528, 1479, and 1265. ¹H NMR (250 MHz, DMSO-*d*₆) $\delta = 9.47$ (s, 1H), 8.62–8.50 (m, 2H), 8.31 (s, 1H), 7.83 (d, $J = 8.1$ Hz, 1H), 7.66 (d, $J = 7.6$ Hz, 2H), 7.57–7.34 (m, 7H), 7.14–7.05 (m, 1H), 5.52 (s, 1H). ¹³C NMR (62.5 MHz, DMSO-*d*₆) $\delta = 164.52$, 152.83, 149.74, 145.08, 137.11, 133.10, 132.29, 130.71, 128.58, 127.64, 126.55, 126.32, 124.10, 123.20, 122.31, 122.11, 119.92, 117.19, 114.16, 97.94, 44.49, 40.98, 40.65, 40.32, 39.98, 39.65, 39.32, 38.98. ESI-mass: $m/z = 376$.

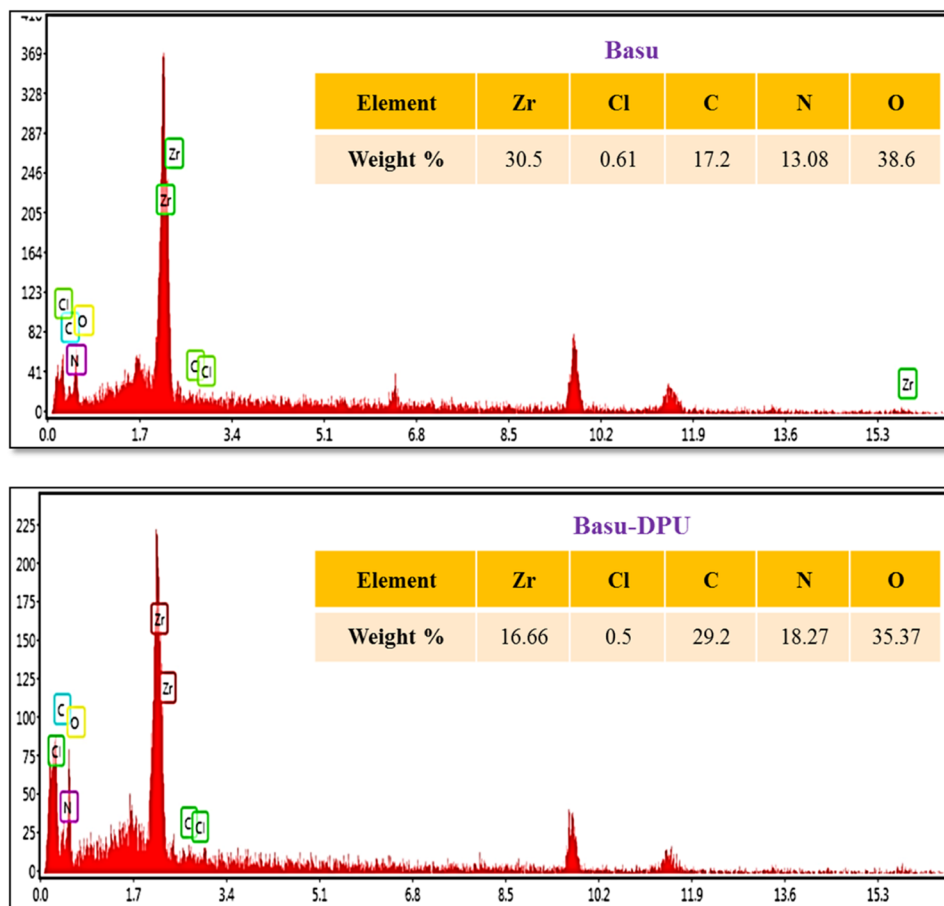


Figure 4. EDX analysis of Basu and Basu-DPU.

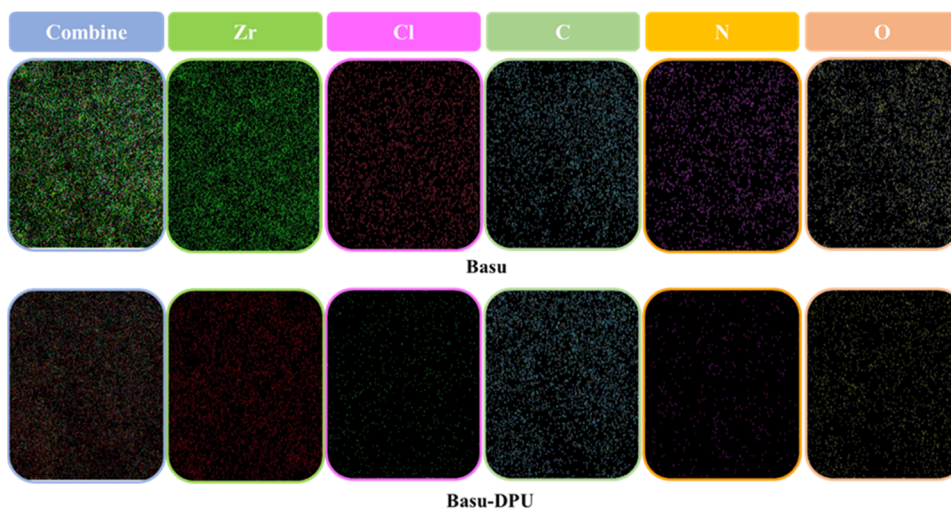
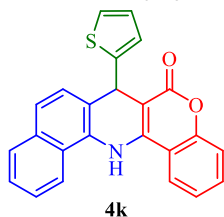


Figure 5. Elemental mapping analysis of Basu and Basu-DPU.

2.4.11. 7-(Thiophen-2-yl)-7,14-dihydro-6H-benzo[h]-chromeno[4,3-b]quinolin-6-one (**4k**).



Yellow solid, mp 204 °C, IR (KBr, cm^{-1}): 3294, 3060, 2927, 1676, 1621, 1521, 1394, and 1269. ^1H NMR (250 MHz, $\text{DMSO}-d_6$) δ = 9.69 (s, 1H), 8.63 (d, J = 8.2 Hz, 1H), 8.56 (d, J = 7.9 Hz, 1H), 7.89 (d, J = 12.2 Hz, 2H), 7.64 (d, J = 7.6 Hz, 3H), 7.49–7.38 (m, 3H), 7.19 (d, J = 4.8 Hz, 1H), 6.82 (dt, J = 6.8, 3.5 Hz, 2H), 5.68 (s, 1H), 2.05 (s, 8H), 1.00 (s, 6H). ^{13}C NMR (62.5 MHz, $\text{DMSO}-d_6$) δ = 160.98, 152.77, 151.19, 144.70, 136.34, 134.87, 133.28, 132.32, 131.02, 128.61, 127.76, 127.16, 126.66, 126.36, 124.89, 124.34, 124.13, 123.93, 123.50,

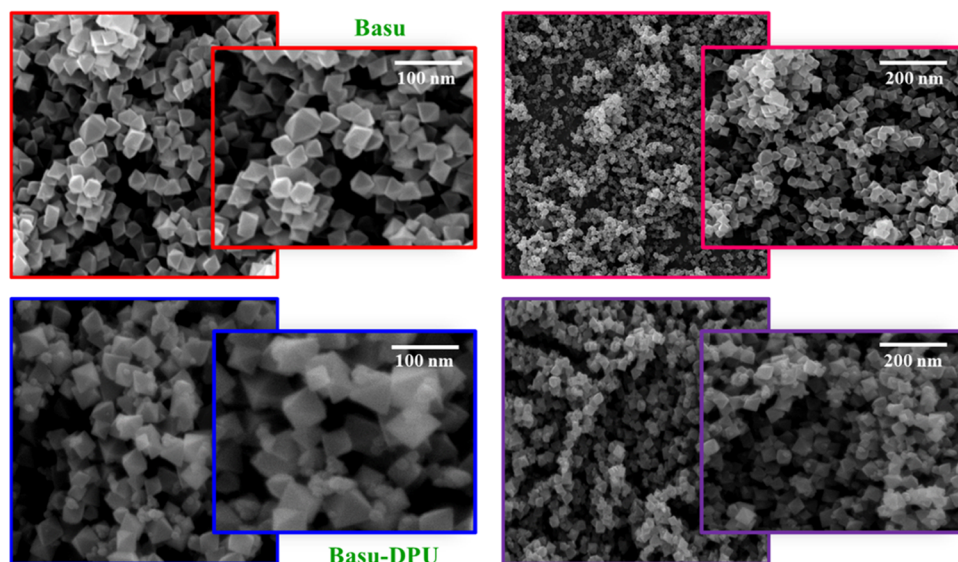
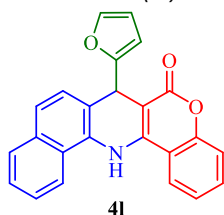


Figure 6. SEM images of Basu and Basu-DPU.

122.55, 120.37, 117.21, 49.04, 41.00, 40.67, 40.34, 40.00, 39.67, 39.34, 39.00, 37.09. ESI-mass: $m/z = 381$.

2.4.12. 7-(Furan-2-yl)-7,14-dihydro-6H-benzo[h]-chromeno[4,3-b]quinolin-6-one (**4I**).



Brown solid, mp > 300 °C, IR (KBr, cm^{-1}): 3407, 2925, 1699, 1627, 1525, 1401, and 1263. ^1H NMR (250 MHz, $\text{DMSO}-d_6$) $\delta = 9.62$ (s, 1H), 8.59 (s, 1H), 7.92 (s, 2H), 7.64 (d, $J = 7.8$ Hz, 2H), 7.55 (s, 2H), 7.45 (d, $J = 8.6$ Hz, 3H), 7.39 (s, 1H), 6.25 (s, 1H), 6.09 (s, 1H), 5.49 (s, 1H). ^{13}C NMR (62.5 MHz, $\text{DMSO}-d_6$) $\delta = 161.06, 157.42, 152.58, 142.30, 133.13, 132.59, 130.60, 128.62, 127.46, 126.75, 126.59, 124.41, 123.67, 122.97, 121.92, 118.01, 117.22, 113.78, 110.96, 105.49, 95.38, 48.92, 40.46, 40.12, 39.79, 39.45, 39.12, 38.78, 38.45, 35.82$. ESI-mass: $m/z = 365$.

3. RESULTS AND DISCUSSION

3.1. Characterization of Basu and Basu-DPU. Various techniques such as FTIR, ^{13}C NMR, EDX, elemental mapping, XRD, SEM, TGA/DTA, and BET were employed to characterize the Basu and Basu-DPU frameworks.

3.1.1. Characterization by FTIR. The FTIR spectra of ZrCl_4 , BDA4BPpy, BDC- NH_2 , Basu, and Basu-DPU are comparatively demonstrated in Figure 2. The FTIR spectrum of the BDA4BPpy ligand indicates the two peaks at 1597 and 1631 cm^{-1} , which can be assigned to the C=C and C=N bonds. In the curve BDC- NH_2 , the peaks appeared at 3400 and 3514 cm^{-1} related to the symmetric and asymmetric vibrations of N-H bonds. The peaks observed at 1697, 1596, and 1497 cm^{-1} belong to the stretching vibration of the C=O bond of the carboxylic acid group and the C=C bonds of the aromatic ring, respectively. According to the fingerprint pattern of Basu, the prominent bands appeared at 3499, 3382, 1666, 1587, 1446, 1270, and 772 cm^{-1} were attributed to the symmetric

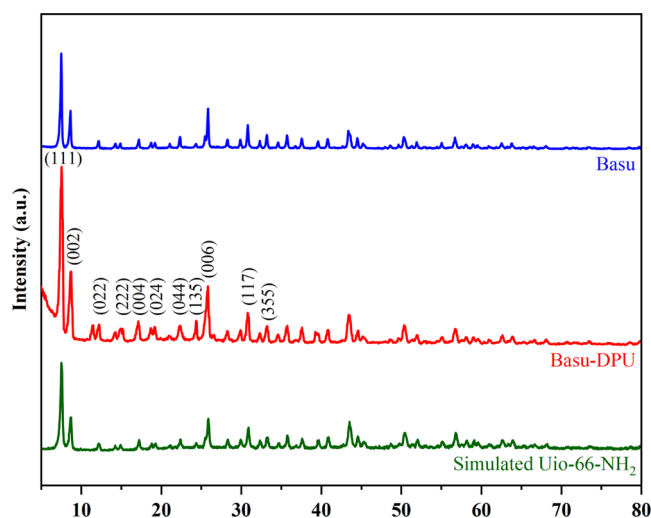


Figure 7. XRD patterns of Basu, Basu-DPU, and UiO-66- NH_2 .

and asymmetric vibrations of the amino groups, the stretching modes of C=O, aromatic C-C, $\text{C}_{\text{aromatic}}-\text{N}$, and Zr-O bonds, respectively, which confirms the successful construction of the desired MOF. After modifications of Basu, the fingerprint pattern of Basu-DPU transfers to a lower frequency, and the presence of the stretching vibration of the C=O amide at 1652 cm^{-1} indicates that the NH_2 groups well bonded to the phenyl isocyanate during the modification.

3.1.2. Characterization by ^{13}C NMR. The structure of the Basu framework was studied by the ^{13}C NMR spectroscopy method reported by the Feng group.³³ The UiO-66- NH_2 framework includes eight characteristic peaks at 114, 116, 118, 131, 135, 150, 167, and 169 ppm, which are related to the BDC- NH_2 ligand.³⁴ As shown in Figure 3, the synthesized Basu framework has twelve peaks at 116, 118, 119, 121, 132, 135, 146, 163, 167, 168, 169, and 173 ppm, which confirms the Basu framework formation.

3.1.3. Characterization by EDX and Elemental Mapping Analysis. The elemental peaks in energy-dispersive X-ray (EDX) spectroscopy confirmed the presence of Zr, Cl, C, N, and O elements in Basu and Basu-DPU frameworks (Figure 4).

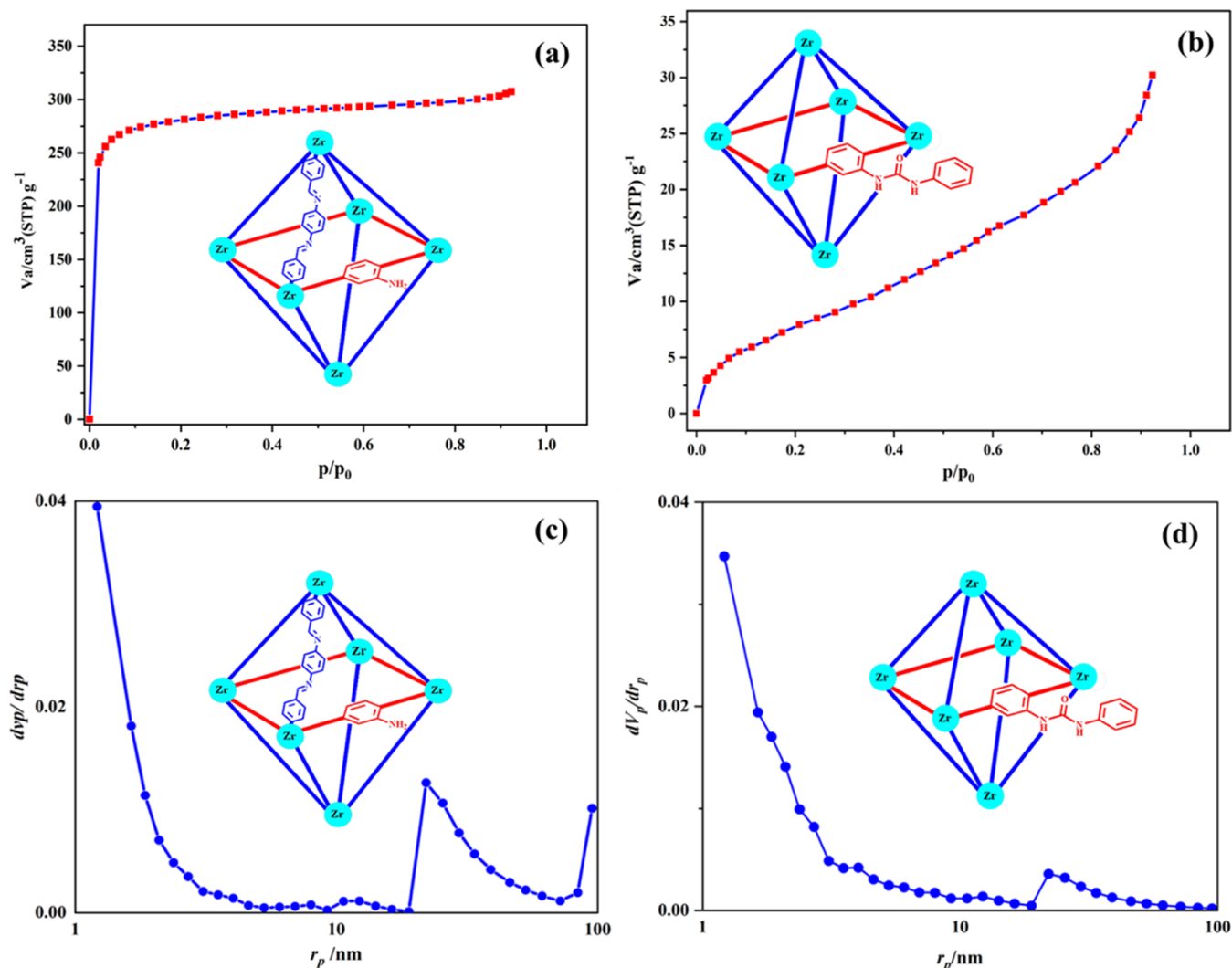


Figure 8. Nitrogen adsorption–desorption curve (BET) of (a) Basu and (b) Basu-DPU and the BJH adsorption curve of (c) Basu and (d) Basu-DPU.

Table 1. Results from the BET Measurements of Basu and Basu-DPU

no	parameter	Basu	Basu-DPU
1	a_s (m^2/g)	1107.1	528.8
2	V_m (cm^3/g)	254.3	121.5
3	total pore volume (cm^3/g)	0.80	0.32
4	mean pore diameter (nm)	2.90	2.45

In addition, EDX mappings represent the homogeneous distribution of all elements in both frameworks (Figure 5).

3.1.4. Characterization by the FESEM Analysis. The morphology of synthesized frameworks was explored by field-emission scanning electron microscopy (FESEM). The FESEM images showed the octahedron structure, uniform size, and homogeneous particle distribution for the Basu framework (Figure 6). Besides, the FESEM images of Basu and Basu-DPU displayed that the morphology of the primary MOF was kept well and considerably after the postmodification with phenyl isocyanate.

3.1.5. Characterization by XRD. The XRD patterns of Basu, Basu-DPU, and UiO-66-NH₂ are compared in Figure 7. As can be seen, the XRD patterns of both Basu and Basu-DPU

frameworks are similar to UiO-66-NH₂ with the difference that their peaks have shifted to a lower degree with high intensity. The characteristic peaks at $2\theta = 7.5, 8.7, 12.2, 15, 17.1, 19.1, 22.4, 24.3, 25.8, 30.8,$ and 33.2 correspond to the (111), (002), (022), (222), (004), (024), (044), (135), (006), (117), and (335) diffraction, respectively.³⁵ According to the Scherrer equation ($D = K\lambda/(\beta \cdot \cos \theta)$), the average crystallite size of Basu-DPU was found to be about 17.03 nm.

3.1.6. Characterization by BET. The specific surface area of Basu and Basu-DPU was characterized using the N₂ adsorption–desorption analysis. The results are presented in Figure 8a,b, and the corresponding detailed parameters are listed in Table 1.

According to the IUPAC classification of adsorption isotherms,³⁶ the N₂ isotherms of Basu and Basu-DPU are similar to type I(b) and type II, respectively. As observed from the BET analysis results, the surface area, pore volume (V_m), and total pore volume (cm^3/g) of Basu are 1107.1 m^2/g , 254.36, and 0.8038 cm^3/g , respectively. Compared to the primary MOF, the surface area, pore volume (V_m), and total pore volume (cm^3/g) of Basu-DPU have been reduced to 528.8 m^2/g , 121.5, and 0.32 cm^3/g , respectively, which can be

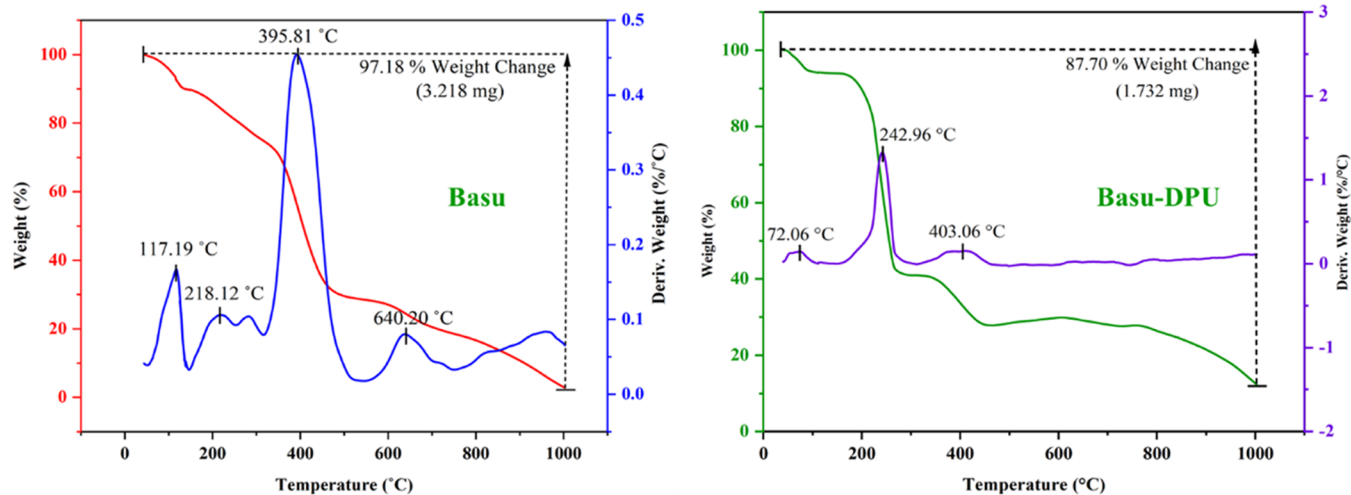


Figure 9. TGA-DTA curve of the Basu and Basu-DPU frameworks.

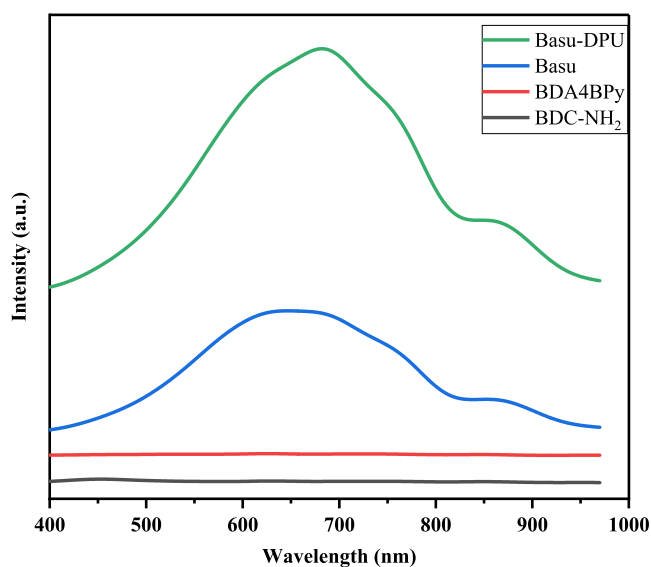


Figure 10. Fluorescence characteristic peaks of BDC-NH₂, BDA4BPy, Basu, and Basu-DPU.

attributed to the presence of the larger PhNCO tags than amine groups.

Also, the obtained BJH adsorption indicated that the pore size of Basu and Basu-DPU is about 1.21 nm (Figure 8c,d).

3.1.7. Characterization by TGA-DTA. Moreover, the thermogravimetric analysis (TGA-DTG) was carried out under airflow to investigate the thermal behavior of the Basu and Basu-DPU frameworks (Figure 9). The obtained results were compared with the results reported for the UiO-66-NH₂ framework.

According to previous reports, UiO-66-NH₂ shows a three-step weight loss. The weight loss (22%) around 100 °C was attributed to the removal of surface water molecules. The weight loss (3–5%) around 200 °C was due to the loss of DMF molecules from the pores and also the loss of water molecules coordinated in the cage within the MOF. The third weight loss was observed at 350 °C, which can be ascribed to the collapse of the structure of MOFs and buried the organic linkers.³⁷

Compared to UiO-66-NH₂, Basu indicates four-step weight loss. As seen in Figure 9, the weight loss (~10–16%) between

Table 2. Optimization of the Reaction Conditions for the Synthesis of 4(a–l)

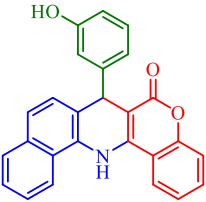
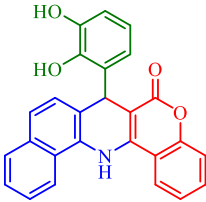
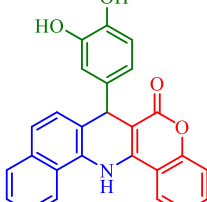
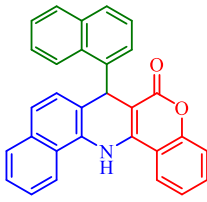
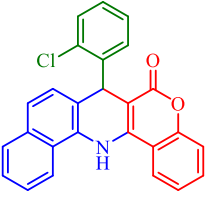
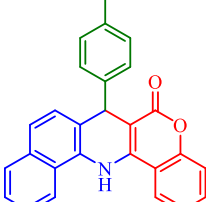
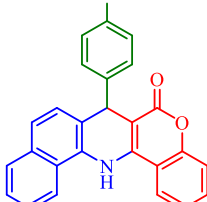
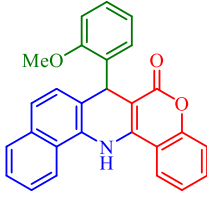
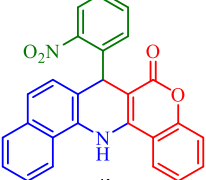
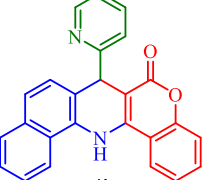
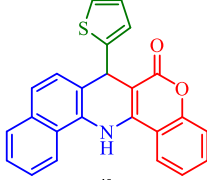
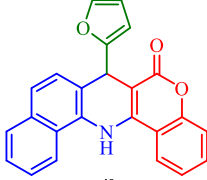
entry	condition	catalyst	catal. amount (mg)	time (min)	yield (%)
1	solvent-free, 110 °C	Basu-DPU	10	10	95
2	solvent-free, 110 °C	Basu-DPU	20	10	88
3	solvent-free, 110 °C	Basu-DPU	30	10	86
4	solvent-free, 110 °C	catalyst-free	-	10	15
5	EtOH, reflux	Basu-DPU	10	10	75
6	CH ₃ CN, reflux	Basu-DPU	10	10	23
7	EtOAc, reflux	Basu-DPU	10	10	15
8	DMF, 110 °C	Basu-DPU	10	10	20
9	CH ₂ Cl ₂ , reflux	Basu-DPU	10	10	-
10	solvent-free, 110 °C	Basu	10	10	83
11	solvent-free, 110 °C	UiO-66-NH ₂	10	10	75
12	solvent-free, 110 °C	<i>p</i> -TSA	10	10	50
13	solvent-free, 110 °C	L-proline	0.01"	10	40
14	solvent-free, 110 °C	Et ₃ N	0.01"	10	25
15	solvent-free, 110 °C	piperidine	0.01"	10	28

Table 3. Purification of 4(a–l)

product	method	product	method
4a	washing with ethanol	4g	recrystallization in DMF
4b	recrystallization in DMF	4h	recrystallization in DMF
4c	recrystallization in DMF	4i	recrystallization in DMF
4d	recrystallization in DMF	4j	recrystallization in DMF
4e	recrystallization in DMF	4k	TLC plate
4f	washing with acetone	4l	TLC plate

117–218 °C was ascribed to the loss of solvent molecules residing in the open channels and the physically adsorbed moisture. The weight loss (~47%) was observed around 395 °C due to the decomposition of organic moieties. The next weight loss (~25%) at 640 °C can be attributed to the

Table 4. Synthesis of 4(a–l) Using the Basu-DPU Framework^a

 <p>4a M.P. (°C) = >300 Time (min) = 10 Yield (%) = 95, AE (%) = 90.4</p>	 <p>4b M.P. (°C) = 280–283 Time (min) = 15 Yield (%) = 68, AE (%) = 63</p>	 <p>4c M.P. (°C) = >300 Time (min) = 12 Yield (%) = 81, AE (%) = 74</p>	 <p>4d M.P. (°C) = >300 Time (min) = 15 Yield (%) = 91.7, AE (%) = 84.7</p>
 <p>4e M.P. (°C) = >300 Time (min) = 20 Yield (%) = 88, AE (%) = 81</p>	 <p>4f M.P. (°C) = >300 Time (min) = 10 Yield (%) = 95.9, AE (%) = 88.4</p>	 <p>4g M.P. (°C) = >300 Time (min) = 10 Yield (%) = 93.8, AE (%) = 86.3</p>	 <p>4h M.P. (°C) = >300 Time (min) = 13 Yield (%) = 86, AE (%) = 79.5</p>
 <p>4i M.P. (°C) = >300 Time (min) = 25 Yield (%) = 83.3, AE (%) = 81.5</p>	 <p>4j M.P. (°C) = >300 Time (min) = 20 Yield (%) = 90, AE (%) = 82</p>	 <p>4k M.P. (°C) = 204 Time (min) = 15 Yield (%) = 73.9, AE (%) = 64.9</p>	 <p>4l M.P. (°C) = >300 Time (min) = 25 Yield (%) = 68.4, AE (%) = 62.5</p>

^aReaction conditions: 4-hydroxycumarine (1.0 mmol), 1-naphthylamine (1.0 mmol), aldehyde (1.0 mmol), and Basu-DPU (10 mg) under solvent-free conditions.

decomposition of the framework. Moreover, about 2.82% of the initial mass remains at 1000 °C.

Based on the results obtained from the TGA-DTG analysis of Basu-DPU, the weight loss (6%) was observed below 200 °C due to solvent molecules residing in the open channels and the physically adsorbed moisture. The weight loss of 53% in the temperature range of 200–300 °C can be attributed to guest molecules and the dehydroxylation of zirconium clusters. The weight loss of 28% from 300 to 1000 °C can be ascribed to the decomposition of the framework. The amount of char was calculated to be 12.3% at 1000 °C.

3.1.8. Characterization by Fluorescence. In another study, the fluorescence properties of the Basu and Basu-DPU frameworks were measured in DMF solution with a concentration of 200 ppm at room temperature. As can be seen in Figure 10, in the absence of metal ions, fluorescence of Basu and Basu-DPU is probably quenched by the occurrence of a photoinduced electron transfer (PET) process due to the presence of a lone pair of electrons of nitrogen donor atoms in Basu and Basu-DPU. The observed fluorescence enhancement was explained by blocking the photoinduced electron transfer pathway in Basu and Basu-DPU due to binding with Zr⁴⁺. The PET process is prevented by the complexation of Basu and Basu-DPU with Zr ions. The fluorescence characteristic peaks that appeared around 655 and 864 nm belong to the Basu

framework and the 685 and 862 nm peaks belong to the Basu-DPU framework. The fluorescence characteristic peaks of Basu and Basu-DPU frameworks tend to first intensify and then weaken. Moreover, the structural modification causes the difference in fluorescence peak intensity and a large blue shift in the direction of a longer wavelength concerning that of Basu. This implies that the substituent DPU has a considerable influence on the fluorescence intensity and the fluorescence wavelength of this framework.

3.2. Optimization of the Reaction Conditions. After preparation and complete characterization of the Basu-DPU framework, we used it as the catalyst for the synthesis of diverse 4(a–l). To attain the optimized conditions, the reaction of 4-hydroxycumarine 1, 1-naphthylamine 2, and 3-hydroxybenzaldehydes 3 in the presence of the Basu-DPU framework was chosen as a model reaction to gain the best reaction conditions. Herein, the effect of the amount of catalyst and solvent was studied.

Since different amounts of catalysts have a significant effect on the performance of catalyst systems, we studied the effect of the amount of catalyst on the reaction with three different amounts of catalysts of 10, 20, and 30 mg in the first step. As shown in Table 2, increasing the amount of catalyst does not have a significant effect on its performance. Hence, due to the economic aspect, the amount of catalyst of 10 mg was selected

Scheme 3. Plausible Mechanism for the Synthesis of 4(a–l) by Basu-DPU

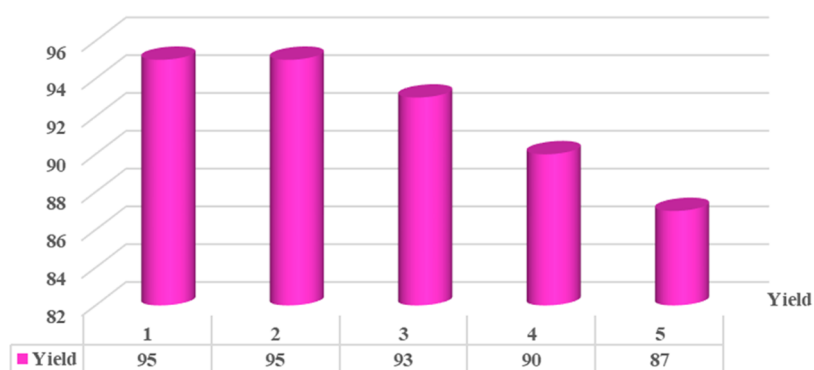
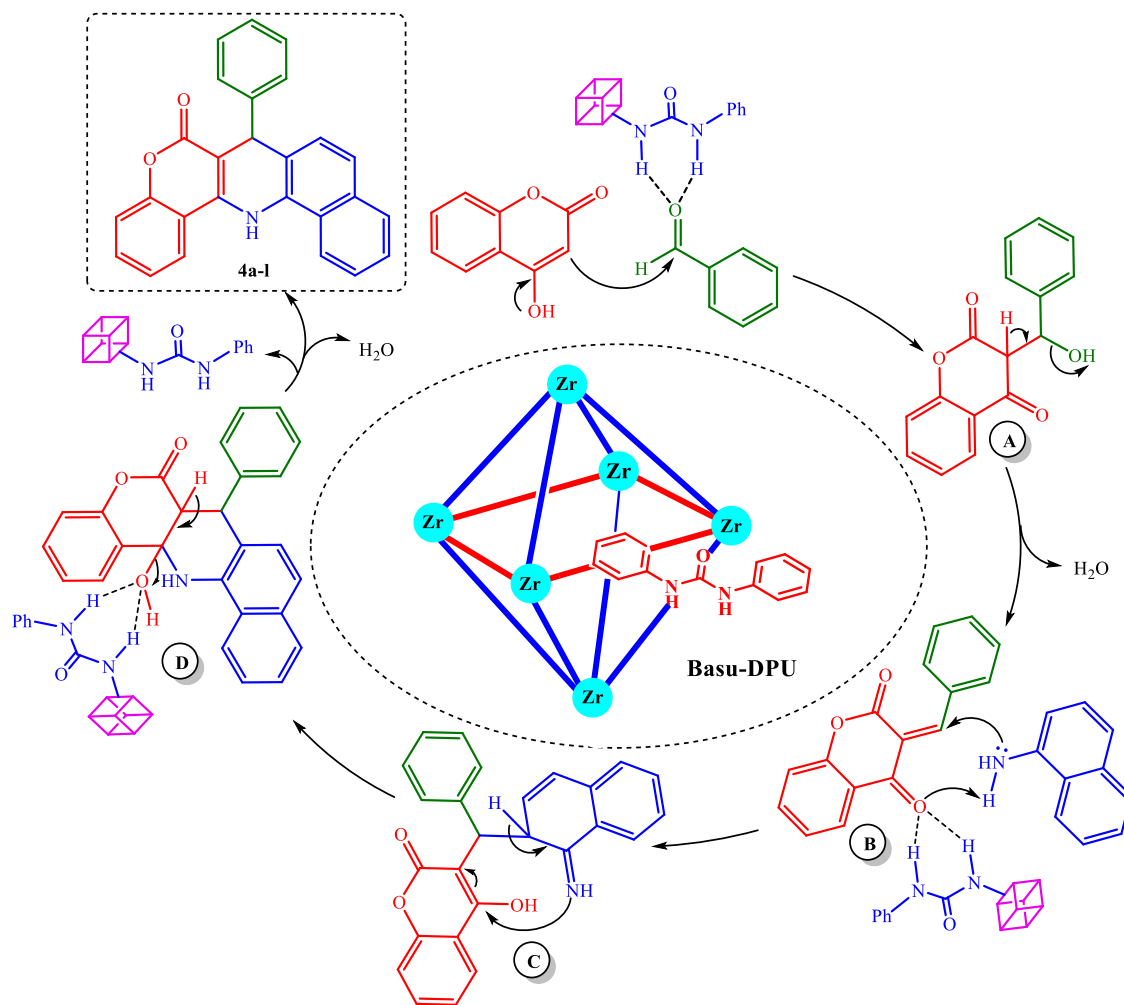


Figure 11. Recyclability of the Basu-DPU framework.

as the best catalyst concentration under solvent-free conditions at 110 °C. In the next step, the model reaction was done in the presence of different solvents and temperatures. According to the obtained results, the polarity of the solvent had a considerable effect. For example, a nonpolar solvent such as CH_2Cl_2 had no effect, while a polar solvent such as EtOH was the most efficient solvent with up to 89% yield. The polar aprotic solvents CH_3CN and DMF had relatively low performance compared to the protic solvent EtOH.

To demonstrate the ability of the synthesized catalyst, the model reaction was also carried out with several known

catalysts, which shows that Basu-DPU is more effective than other catalysts.

3.3. Synthesis of Diverse 4(a–l). With optimal reaction conditions in hand (10 mg of Basu-DPU was employed as the catalyst under solvent-free conditions at 110 °C), the scope and generality of the presented method are studied to synthesize a range of new biological interest candidates 6*H*-chromeno- [4,3-*b*]quinolin-6-ones (**4a–l**) using 4-hydroxycumarine **1**, 1-naphthylamine **2**, and aromatic aldehydes (heterocycle, bearing electron-donating and electron-withdrawing groups) **3a–l**. The obtained products were purified

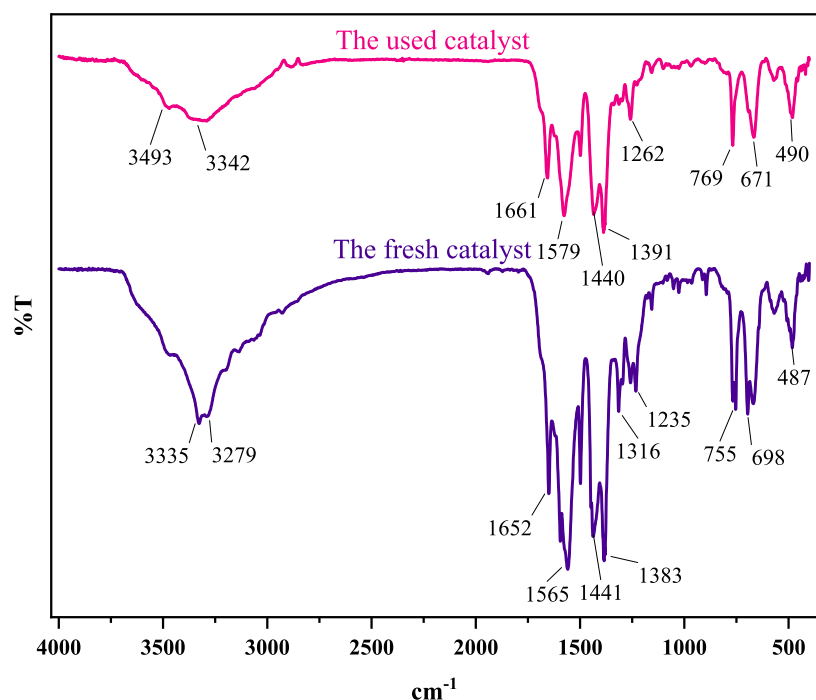


Figure 12. FTIR spectra the fresh and used Basu-DPU catalyst.

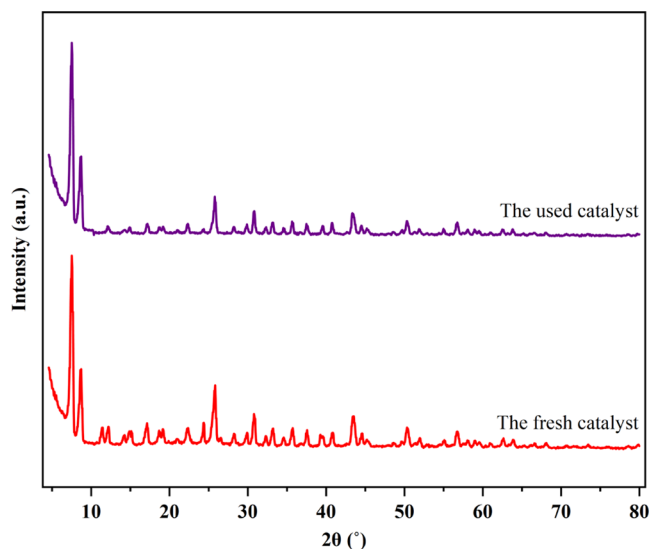


Figure 13. XRD patterns of the fresh and used Basu-DPU catalyst.

by recrystallization in DMF, washing with ethanol and acetone, or using thin-layer chromatography plates (Table 3).

The achieved data showed that the electron-poor or electron-rich groups do not affect the process of reactions, and Basu-DPU is a suitable catalyst for the preparation of desired products in high to excellent yields with high atom efficiency (AE) and short reaction times (Table 4).

3.4. Proposed Mechanism for the Synthesis of Diverse 4(a–l). A plausible mechanism for explaining this one-pot strategy is presented in Scheme 3. The proposed mechanism begins with the condensation between 4-hydroxycoumarin and the activated aldehyde to give the intermediate A, which subsequently loses H₂O, to afford the intermediate B. Afterward, a nucleophilic attack of 1-naphthylamine to the activated intermediate B gives the

intermediate C, which readily undergoes a subsequent intramolecular cyclization to produce the intermediate D. Finally, the resulting intermediate D with loss of H₂O generates the target molecules 4(a–l).

3.5. Reusability of the Basu-DPU Framework. In a separate study, we studied the easy recyclability of this catalyst for the synthesis of target molecule 4a under optimal reaction conditions. At the end of each run, the solid was dissolved in 10 mL of DMF and centrifuged to separate the Basu-DPU catalyst. The separated catalyst was washed with EtOH, dried, and reused for the next run. The results indicated that Basu-DPU could be reused 5 times without any considerable decrease in yield reaction (Figure 11).

Moreover, the used catalyst was evaluated after the fifth catalytic cycle by the FTIR, XRD, and SEM techniques. As shown in Figure 12, the index peaks of the synthesized framework involving symmetric and asymmetric vibrations of the amino groups (3335 and 3279 cm⁻¹), the stretching vibration of C=O (1652 cm⁻¹), and the stretching vibration of aromatic C–C (1441 cm⁻¹) and Zr–O (755 cm⁻¹) were preserved in the recycled catalyst, which demonstrates the stability of the recycled catalyst. On the other hand, the XRD spectrum of the used Basu-DPU catalyst shows that the crystalline phase is preserved (Figure 13). In addition, the SEM images show that the structure of the catalyst remained intact (Figure 14).

4. CONCLUSIONS

In conclusion, we presented the Basu-DPU catalyst as a new two-fold interpenetrated pillar-layered metal–organic framework. According to the achieved images of FESEM analysis, Basu-DPU has an octahedron structure. Fluorescence studies show that Basu and Basu-DPU are probably quenched by the occurrence of a photoinduced electron transfer (PET) process in the absence of metal ions due to the presence of a line pair of electrons of nitrogen donor atoms in Basu and Basu-DPU.

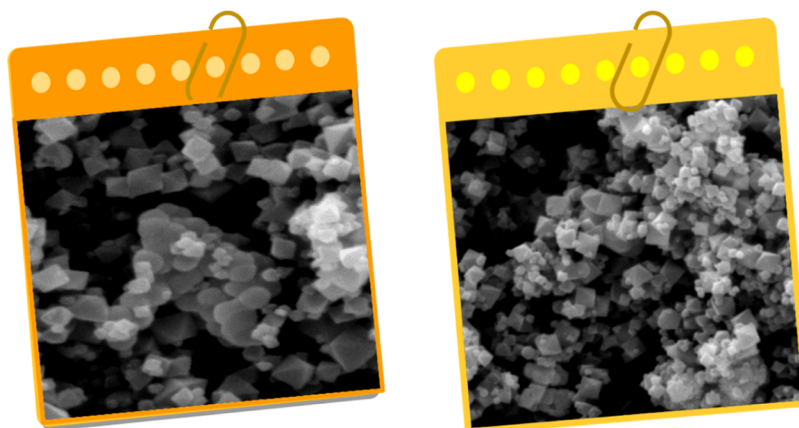


Figure 14. SEM images of the used Basu-DPU catalyst.

Basu-DPU as an efficient catalyst was applied to synthesize new biological interest candidates **4(a–l)**. Low catalyst loading, recyclability, and reusability of the catalyst, short reaction times, high yields, good atom efficiency, adaptability with different functional groups, and simple work-up are the most attractive features of the presented study. The catalyst indicated high recyclability for more than five cycles without any considerable decrease in yield reaction. Moreover, FTIR, XRD, and SEM analyses of the used catalyst demonstrate that the structure and reactivity of the catalyst remained intact with a poor decrease in its efficiency in comparison to the fresh catalyst.

■ ASSOCIATED CONTENT

SI Supporting Information

The Supporting Information is available free of charge at <https://pubs.acs.org/doi/10.1021/acsomega.3c01793>.

Copies of the FTIR, ^1H NMR, and ^{13}C NMR spectra for all compounds as well as the mass spectra for new compounds (PDF)

■ AUTHOR INFORMATION

Corresponding Author

Davood Habibi – Department of Organic Chemistry, Faculty of Chemistry, Bu-Ali Sina University, Hamedan 6517838683, Iran; orcid.org/0000-0002-2386-8502; Phone: +98 81 38380922; Email: davood.habibi@gmail.com, dhabibi@basu.ac.ir; Fax: +98 81 38380709

Authors

Masoumeh Beiranvand – Department of Organic Chemistry, Faculty of Chemistry, Bu-Ali Sina University, Hamedan 6517838683, Iran

Hosein Khodakarami – Department of Organic Chemistry, Faculty of Chemistry, Bu-Ali Sina University, Hamedan 6517838683, Iran

Complete contact information is available at:

<https://pubs.acs.org/doi/10.1021/acsomega.3c01793>

Notes

The authors declare no competing financial interest.

■ ACKNOWLEDGMENTS

The authors thank the Bu-Ali Sina University for the support of this work.

■ REFERENCES

- (1) (a) Yuan, S.; Qin, J. S.; Zou, L.; Chen, Y. P.; Wang, X.; Zhang, Q.; Zhou, H. C. Thermo-dynamically guided synthesis of mixed-linker Zr-MOFs with enhanced tenability. *J. Am. Chem. Soc.* **2016**, *138*, 6636–6642. (b) Wang, T. C.; Bury, W.; Gómez-Gualdrón, D. A.; Vermeulen, N. A.; Mondloch, J. E.; Deria, P.; Farha, O. K.; et al. Ultrahigh surface area zirconium MOFs and insights into the applicability of the BET theory. *J. Am. Chem. Soc.* **2015**, *137*, 3585–3591. (c) Deria, P.; Gómez-Gualdrón, D. A.; Hod, I.; Snurr, R. Q.; Hupp, J. T.; Farha, O. K. Framework-topology-dependent catalytic activity of zirconium-based (porphyrinato) zinc(II) MOFs. *J. Am. Chem. Soc.* **2016**, *138*, 14449–14457. (d) Li, Y.; Pascal, K.; Jin, X. J. Ni-Mo modified metal-organic frameworks for high-performance super capacitance and enzymeless H_2O_2 detection. *CrystEngComm* **2020**, *22*, 5145–5161. (e) Hu, Z.; Wang, Y.; Zhao, D. The chemistry and applications of hafnium and cerium(IV) metal-organic frameworks. *Chem. Soc. Rev.* **2021**, *50*, 4629–4683.
- (2) Altintas, C.; Avci, G.; Daglar, H.; Azar, A. N. V.; Erucar, I.; Velioglu, S.; Keskin, S. An extensive comparative analysis of two MOF databases: high-throughput screening of computation-ready MOFs for CH_4 and H_2 adsorption. *J. Mater. Chem. A* **2019**, *7*, 9593–9608.
- (3) Wen, M.; Li, G.; Liu, H.; Chen, J.; An, T.; Yamashita, H. Metal-organic framework-based nanomaterials for adsorption and photocatalytic degradation of gaseous pollutants: recent progress and challenges. *Environ. Sci. Nano* **2019**, *6*, 1006–1025.
- (4) Lashaki, M. J.; Khiavi, S.; Sayari, A. Stability of amine-functionalized CO_2 adsorbents: a multifaceted puzzle. *Chem. Soc. Rev.* **2019**, *48*, 3320–3405.
- (5) Li, X.; Liu, Y.; Wang, J.; Gascon, J.; Li, J.; Van der Bruggen, B. Metal-organic frameworks-based membranes for liquid separation. *Chem. Soc. Rev.* **2017**, *46*, 7124–7144.
- (6) Lan, T.; Li, L.; Chen, Y.; Wang, X.; Yang, J.; Li, J. Opportunities, and critical factors of porous metal-organic frameworks for industrial light olefins separation. *Mater. Chem. Front.* **2020**, *4*, 1954–1984.
- (7) Yang, Q.; Xu, Q.; Jiang, H. L. Metal-organic frameworks meet metal nanoparticles: synergistic effect for enhanced catalysis. *Chem. Soc. Rev.* **2017**, *46*, 4774–4808.
- (8) Guo, J.; Qin, Y.; Zhu, Y.; Zhang, X.; Long, C.; Zhao, M.; Tang, Z. Metal-organic frameworks as catalytic selectivity regulators for organic transformations. *Chem. Soc. Rev.* **2021**, *50*, 5366–5396.
- (9) Liang, Z.; Wang, H. Y.; Zheng, H.; Zhang, W.; Cao, R. Porphyrin-based frameworks for oxygen electrocatalysis and catalytic reduction of carbon dioxide. *Chem. Soc. Rev.* **2021**, *50*, 2540–2581.
- (10) Stassen, I.; Burtch, N.; Talin, A.; Falcaro, P.; Allendorf, M.; Ameloot, R. An updated roadmap for the integration of metal-organic frameworks with electronic devices and chemical sensors. *Chem. Soc. Rev.* **2017**, *46*, 3185–3241.
- (11) Zhu, H.; Liu, D. The synthetic strategies of metal-organic framework membranes, films and 2D MOFs and their applications in devices. *J. Mater. Chem. A* **2019**, *7*, 21004–21035.

- (12) Cai, M.; Qin, L.; You, L.; Yao, Y.; Wu, H.; Zhang, Z.; Ni, J.; et al. Functionalization of MOF-5 with mono-substituents: effects on drug delivery behavior. *RSC Adv.* **2020**, *10*, 36862–36872.
- (13) Erucar, I.; Keskin, S. Computational investigation of metal-organic frameworks for storage and delivery of anticancer drugs. *J. Mater. Chem. B* **2017**, *5*, 7342–7351.
- (14) Yang, J.; Wang, H.; Liu, J.; Ding, M.; Xie, X.; Yang, X.; Miao, Y.; et al. Recent advances in nanosized metal organic frameworks for drug delivery and tumor therapy. *RSC Adv.* **2021**, *11*, 3241–3263.
- (15) Zhang, Y. X.; Li, B. X.; Lin, H.; Ma, Z.; Wu, X. T.; Zhu, Q. L. Impressive second harmonic generation response in a novel phase-matchable NLO-active MOF derived from achiral precursors. *J. Mater. Chem. C* **2019**, *7*, 6217–6221.
- (16) Zhai, Q. G.; Bai, N.; Li, S.; Bu, X.; Feng, P. Design of pore size and functionality in pillar-layered Zn-triazolate-dicarboxylate frameworks and their high CO₂/CH₄ and C₂ hydro-carbons/CH₄ selectivity. *Inorg. Chem.* **2015**, *54*, 9862–9868.
- (17) Zhou, H. F.; Liu, B.; Wang, H. H.; Hou, L.; Zhang, W. Y.; Wang, Y. Y. Construction of highly porous pillared metal-organic frameworks: Rational synthesis, structure, and gas sorption properties. *Inorg. Chem.* **2017**, *56*, 9147–9155.
- (18) Hu, X. L.; Liu, F. H.; Wang, H. N.; Qin, C.; Sun, C. Y.; Su, Z. M.; Liu, F. C. Controllable synthesis of is reticular pillared-layer MOFs: Gas adsorption, iodine sorption and sensing small molecules. *J. Mater. Chem. A* **2014**, *2*, 14827–14834.
- (19) Chen, Z.; Li, P.; Wang, X.; Otake, K. I.; Zhang, X.; Robison, L.; Farha, O. K.; et al. Ligand-directed reticular synthesis of catalytically active missing zirconium-based metal-organic frameworks. *J. Am. Chem. Soc.* **2019**, *141*, 12229–12235.
- (20) Chen, Z.; Hanna, S. L.; Redfern, L. R.; Alezi, D.; Islamoglu, T.; Farha, O. K. Reticular chemistry in the rational synthesis of functional zirconium cluster-based MOFs. *Coord. Chem. Rev.* **2019**, *386*, 32–49.
- (21) Chen, H.; Chen, Z.; Farha, O. K.; Snurr, R. Q. High propane, and isobutane adsorption cooling capacities in zirconium-based metal-organic frameworks predicted by molecular simulations. *ACS Sustainable Chem. Eng.* **2019**, *7*, 18242–18246.
- (22) Shen, G.; Wang, Z.; Huang, X.; Hong, M.; Fan, S.; Lv, X. Palladium/copper co-catalyzed C-H activation and C-C bond regioselective cleavage reaction for the synthesis of fused chromenoquinolines. *Org. Lett.* **2020**, *22*, 8860–8865.
- (23) Weng, Y.; Zhou, H.; Sun, C.; Xie, Y.; Su, W. Copper-catalyzed cyclization for access to 6H-chromeno[4,3-b]quinolin-6-ones employing DMF as the carbon source. *J. Org. Chem. Res.* **2017**, *82*, 9047–9053.
- (24) Hegab, M. I.; Abdel-Fattah, A. S. M.; Yousef, N. M.; Nour, H. F.; Mostafa, A. M.; Ellithy, M. Synthesis, X-ray structure, and pharmacological activity of some 6,6-disubstituted chromeno[4,3-b]- and chromeno-[3,4-c]quinolines. *Arch. Pharm.* **2007**, *340*, 396–403.
- (25) Wang, X. S.; Zhang, M. M.; Zeng, Z. S.; Shi, D. Q.; Tu, S. J. Clean procedure for synthesis of chromeno[4,3-b]benzo[f]quinolin-6-one derivatives: Reaction of N-arylidene naphthalen-2-amine with 4-hydroxycoumarin in aqueous media. *Synth. Commun.* **2006**, *36*, 2047–2057.
- (26) Weng, Y.; Chen, H.; Li, N.; Yang, L.; Ackermann, L. Electro oxidative metal-free cyclization of 4-arylaminocoumarins with DMF as C1-source. *Adv. Synth. Catal.* **2021**, *363*, 2773–2777.
- (27) Chen, Z.; Bi, J.; Su, W. Synthesis, and antitumor activity of novel coumarin derivatives via a three-component reaction in water. *Chin. J. Chem.* **2013**, *31*, 507–514.
- (28) Singha, R.; Islam, A.; Ghosh, P. One-pot three-component tandem annulation of 4-hydroxy-coumarin with aldehyde and aromatic amines using graphene oxide as an efficient catalyst. *Sci. Rep.* **2021**, *11*, No. 19891.
- (29) Khan, M. N.; Pal, S.; Karamthulla, S.; Choudhury, L. H. Multicomponent reactions for facile access to coumarin-fused dihydroquinolines and quinolines: Synthesis and photo-physical studies. *New J. Chem.* **2014**, *38*, 4722–4729.
- (30) Hosseinzadegan, S.; Hazeri, N.; Maghsoodlou, M. T.; Moghaddam-Manesh, M.; Shirzaei, M. Synthesis and evaluation of biological activity of novel chromeno[4,3-b]quinolin-6-one derivatives by SO₃H-tryptamine supported on Fe₃O₄@SiO₂@CPS as recyclable and bioactive magnetic nanocatalyst. *J. Iran. Chem. Soc.* **2020**, *17*, 3271–3284.
- (31) Vatsadze, S. Z.; Nuriev, V. N.; Chernikov, A. V.; Zyk, N. V. Synthesis of novel linear exo-bidentate bispyridine ligands and their complexes with silver(I) tetrafluoroborate. *Russ. Chem. Bull.* **2002**, *51*, 1957–1958.
- (32) Dong, X. W.; Liu, T.; Hu, Y. Z.; Liu, X. Y.; Che, C. M. Urea post-modified in a metal-organic framework as a catalytically active hydrogen-bond-donating heterogeneous catalyst. *Chem. Commun.* **2013**, *49*, 7681–7683.
- (33) Zhang, Y.; Feng, X.; Li, H.; Chen, Y.; Zhao, J.; Wang, S.; Wang, L.; Wang, B. Photoinduced post-synthetic polymerization of a metal-organic framework toward a flexible stand-alone membrane. *Angew. Chem., Int. Ed.* **2015**, *54*, 4259–4263.
- (34) Ghobakhloo, F.; Azarifar, D.; Mohammadi, M.; Keypour, H.; Zeynali, H. Copper (II) Schiff-base complex modified UiO-66-NH₂ (Zr)metal-organic framework catalysts for Knoevenagel condensation–Michael addition–cyclization reactions. *Inorg. Chem.* **2022**, *61*, 4825–4841.
- (35) Wu, R.; Qian, X.; Zhou, K.; Liu, H.; Yadian, B.; Wei, J.; Zhu, H.; Huang, Y. Highly dispersed Au nanoparticles immobilized on Zr-based metal-organic frameworks as hetero-structured catalyst for CO oxidation. *J. Mater. Chem. A* **2013**, *1*, 14294–14299.
- (36) Thommes, M.; Kaneko, K.; Neimark, A. V.; Olivier, J. P.; Rodriguez-Reinoso, F.; Rouquerol, J.; Sing, K. S. Physisorption of gases, with special reference to the evaluation of surface area and pore size distribution (IUPAC Technical Report). *Pure Appl. Chem.* **2015**, *87*, 1051–1069.
- (37) Aghajanzadeh, M.; Zamani, M.; Molavi, H.; Manjili, H. K.; Danafar, H.; Shojaei, A. Preparation of metal-organic frameworks UiO-66 for adsorptive removal of methotrexate from aqueous solution. *J. Inorg. Organomet. Polym. Mater.* **2018**, *28*, 177–186.